Research Article

ADVANCED PHOTONICS

Metasurface-enhanced infrared photothermal microscopy toward ultrasensitive chemical analysis

Danchen Jia,[a,] Steven H. Huang,[b,] Dias Tulegenov,[b] Dashan Dong,[a] Gennady Shvets,[b,] and Ji-Xin Cheng[a,c,d,]

[a]Boston University, Department of Electrical and Computer Engineering, Boston, Massachusetts, United States
[b]Cornell University, School of Applied and Engineering Physics, Ithaca, New York, United States
[c]Boston University, Department of Biomedical Engineering, Boston, Massachusetts, United States
[d]Boston University, Photonics Center, Boston, Massachusetts, United States

Abstract. Infrared spectroscopy with its rich vibrational information plays a crucial role in biochemical sensing. Metasurface-enhanced infrared spectroscopy amplifies the detection sensitivity by enhancing local electromagnetic fields. However, conventional far-field techniques lack the spatial resolution to image the optical response of a single plasmonic nanostructure. In this work, we introduce mid-infrared (mid-IR) photothermal microscopy to map the hot spot distribution and thermal response of a plasmonic metasurface resonant in the mid-IR spectral range. We demonstrate infrared photothermal detection of proteins and drug molecules around a single nanoantenna. Our metasurface-enhanced infrared photothermal microscope achieves a detection limit as low as 0.24 monolayer surface coverage of bovine serum albumin, paving the way for high-throughput, highly sensitive mid-IR analysis of low-abundance molecules.

Keywords: photothermal microscopy; mid-infrared; metasurface; spectroscopy; nanoantenna.

Received Apr. 5, 2025; revised manuscript received Jun. 14, 2025; accepted for publication Jun. 18, 2025; published online Jul. 15, 2025.

[DOI: 10.1117/1.AP.7.5.056001]

1 Introduction

Infrared IR) spectroscopic imaging is a powerful tool in biological, chemical, and material sciences, offering detailed molecular insights.[1 3] However, Fourier transform infrared FTIR) spectroscopy faces challenges in sensitivity, limited by an absorption cross-section of 10 [18] cm^2. Modern infrared spectroscopy, utilizing quantum cascade lasers QCLs) and balanced detection has reached millimolar-level sensitivity.[4] To boost the sensitivity, surface-enhanced infrared absorption SEIRA) spectroscopy has emerged.[5 7] By leveraging plasmonic metasurface, SEIRA significantly enhances the interaction between IR light and target molecules, thus improving the detection sensitivity to the micromolar level and enabling the study of liquid specimens.[8]

The SEIRA technique capitalizes on the strong field confinement induced by resonant coupling between incident IR light and the plasmonic antenna, resulting in the highly localized enhancement of the IR field intensity by up to 10^4-fold at the "hot spot" regions.[9] The versatility has led to a wide range of applications from life sciences to chemical analysis.[10,11] Despite these advances, SEIRA typically relies on far-field reflection or transmission measurements across large areas, which introduces an averaging effect that limits sensitivity, particularly for applications requiring single-molecule detection.[12] Furthermore, although the infrared plasmon resonant modes of metal nanostructures have been studied with photothermal imaging at sub-micrometer spatial resolutions,[13,14] the fundamental physics governing metasurface liquid interactions—specifically, the localized field distributions and temperature dynamics—remain predominantly theoretical.[15] Experimental studies of such interactions are constrained by the spatial resolution limitations of conventional far-field techniques.

*Address all correspondence to Gennady Shvets, gshvets@cornell.edu; Ji-Xin Cheng, jxcheng@bu.edu

†These authors contributed equally to this work.

Near-field IR techniques, such as scattering-type near-field optical microscopy s-SNOM)[16 18] and atomic force microscopy based infrared AFM-IR) spectroscopy,[19 21] have allowed nanoscale visualization of field enhancements. In particular, s-SNOM has been used to map the near field of optical antennas and plasmonic structures, revealing both bright and dark modes.[22] The AFM-IR technique offers a less invasive alternative, providing insights into the near-field properties of plasmonic nanomaterials.[23,24] Nevertheless, these techniques are unsuitable for liquid environments due to significant tip-induced perturbations, limiting their applicability to physiologically relevant biochemical sensing.

Optically detected mid-infrared photothermal MIP) microscopy[25 28] offers a solution to these challenges. Using visible probe lasers to exploit the photothermal effect stemming from the IR absorption of analytes, the MIP effect refines spatial resolution to the visible diffraction limit, which facilitates *in vivo* chemical imaging at subcellular scales. By sensing the IR absorption of molecules with local temperature change, this approach not only boosts sensitivity by suppressing the interference from liquid background but also enables precise, molecular-level measurements in complex biological systems.[29 31] Notably, MIP microscopy has demonstrated the sensitivity to probe micromolar nitrile and azide functional groups in liquid environments.[32,33] Furthermore, the development of widefield MIP microscopy[34 36] and MIP tomography[37 40] has unlocked new possibilities for high-throughput detection.

Here, we advance the detection sensitivity of MIP microscopy from micromolar to nanomolar level via a metasurface-enhanced photothermal sensing architecture. We systematically investigate the contrast mechanisms, including mid-IR field distribution and the thermal dynamics at the metasurface liquid interface. Moreover, we demonstrate spectroscopic detection of protein secondary structure using a single nanoantenna. Our metasurface-enhanced infrared photothermal MEIP) technique achieves 100 nM detection sensitivity for proteins and nitrile molecules, using IR bands at the fingerprint window and the silent window, respectively. These advances open new opportunities for high-throughput, high-sensitivity mid-IR analysis of low-abundance biomolecules and drug molecules in liquid environments.

2 MEIP Principle and Setups

2 1 MEIP Principle

Infrared spectroscopy senses molecules in solution based on the absorbance of IR light. The IR absorbance is proportional to the IR absorption cross-section) of molecules and the molecular concentration c). The pump probe MIP signal of target molecules dissolved in aqueous solutions is generated from the temperature rise via the thermo-optic effect,[27]

$$I_{\mathrm{MIP}} \propto I_{\mathrm{IR}} \frac{c}{mC_p} \frac{\mathrm{d}n}{\mathrm{d}T} I_{\mathrm{probe}}, \quad 1)$$

where I_{IR} is the power of the incident IR light, m is the mass of the heated sample, c is the molar concentration of target molecules, is the absorption cross-section of molecules, C_p is the heat capacity of the system, $\frac{\mathrm{d}n}{\mathrm{d}T}$ is the thermo-optic coefficient of the solution, and I_{probe} is the power of the probe light.

To boost the sensitivity of IR spectroscopy, the plasmonic metasurface is designed to resonate with specific molecular vibrations using gold nanoantenna arrays operating in the mid-infrared mid-IR) regime. In SEIRA, the incident IR field is polarized parallel to the long axis of the nanoantenna to excite localized surface plasmon resonances at mid-IR wavelengths and enhance the IR intensity by up to 3 orders of magnitude,[9]

$$I_{\mathrm{SEIRA}} \propto I_{\mathrm{IR}} \quad E_f{}^2 \quad c\mathrm{d}V, \quad 2)$$

where I_{SEIRA} is the absorbed energy by molecules in SEIRA detection, E_f is the enhancement factor of the IR field produced near the tip of the nanoantenna, and the volume integration is over the nearfield of the nanoantenna. This significant enhancement strengthens the interaction between the IR field and the molecules in the nanoscale hot spots, resulting in an amplified IR absorbance by the order of 10^3. Consequently, low-concentration molecular IR spectra, which are not detectable by conventional FTIR spectroscopy due to the inherently low vibrational absorption cross-section, can be resolved with metasurface enhancement. Despite advances in sensitivity, the reflected IR photons from a single nanoantenna are insufficient for detection with state-of-the-art mid-IR sensors, necessitating synchrotron radiation or an optical parametric oscillator with high pulse energy for improved signal strength.[41,42] Moreover, the limited spatial resolution of SEIRA systems restricts their ability to achieve molecular detection of small objects such as single bio-nanoparticles.

To overcome these challenges, MEIP utilizes a pump probe method to investigate nanoscale thermal dynamics and enable QCL-based IR sensing at the single nanoantenna level [Figs. 1 a) 1 c)]. Upon IR excitation, a strong local field enhancement is generated at the hot spots of the metasurface, transferring energy to the surrounding molecules and exciting their vibrational states. This absorbed energy is subsequently converted into heat through nonradiative decay, resulting in a rise in localized temperature. The temperature gradient induces a change of refractive index in the nanoscale system. Thus, by optically mapping the refractive index changes, the nanoscale thermal behavior of the hot spots can be probed by intensity diffraction tomography, enabling high-resolution IR sensing of molecular vibrations localized around the single nanoantenna [Fig. 1 d)]. The MEIP signal intensity is described as

$$I_{\mathrm{MEIP}} \propto I_{\mathrm{IR}} \quad E_f{}^2 \frac{c}{mC_p} \frac{\mathrm{d}n}{\mathrm{d}T} I_{\mathrm{probe}} \mathrm{d}V \quad 3)$$

Equation 3) shows that MEIP is an integration of MIP and SEIRA. Compared with MIP, the local field enhancement boosts the change of refractive index at the nanoscale, enabling the detection of lower concentration molecules. Compared with SEIRA, the visible probe used in MEIP dramatically improves the spatial resolution, enabling molecular detection at a single nanoantenna level. The photothermal effect of MEIP, specifically the thermo-optic coefficient $\frac{\mathrm{d}n}{\mathrm{d}T}$ in Eq. 3), is influenced by the setup design discussed in the following subsections. In the transmission-mode MEIP tomography system, $\frac{\mathrm{d}n}{\mathrm{d}T}$ is the refractive index change of the solution in hot spots dependent on the temperature rise of the solution. Although in reflection-mode MEIP microscopy, $\frac{\mathrm{d}n}{\mathrm{d}T}$ refers to the visible refractive index change of gold, determined by the temperature variation in the

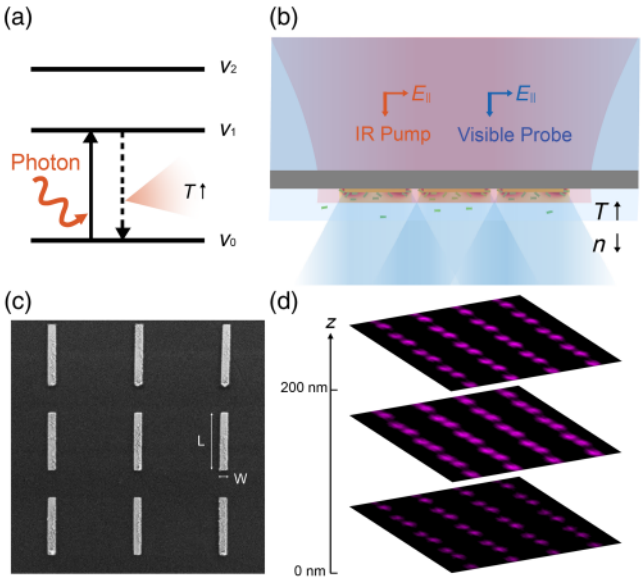

Fig. 1 Concept of MEIP microscopy. (a) Energy diagram of mid-IR photothermal spectroscopy. Molecules absorb IR photons to vibrational excited states and the energy dissipates through nonradiative decay, thus leading to temperature rise. (b) Pump probe detection method of MEIP. A visible wavelength is selected for the probe beam to match the size of the modulated temperature field. Mid-IR field enhancement around nanoantenna results in a rise in localized temperature and thus refractive index decrease of the solutions. (c) SEM image of the metasurface resonant at protein amide-I band. *L*, length of 1.8 μm; *W*, width of 200 nm; and height of 70 nm. (d) MEIP tomography of the hot spots of the metasurface at different depths.

local environment of the nanoantenna. A detailed analysis of the transient photothermal response of the metasurface in solution is presented in Sec. 3.1.

2 2 Metasurface

The metasurface used for MEIP tomography and microscopy comprises rod-shaped gold nanoantenna arrays fabricated on a CaF_2 substrate and engineered to exhibit plasmonic resonance in the mid-IR range. The resonance peak is tuned to match specific vibrational bands of analyte molecules by adjusting the nanoantenna dimensions and the array period. Specifically, the nanoantennas are designed to couple with the amide-I band of proteins, with dimensions of 1.8 μm in length, 200 nm in width, and 70 nm in height. The resonant wavelength, λ_R, is determined by $\lambda_R = n_{\text{eff}} L$, where n_{eff} is the mid-IR effective refractive index of the gold nanoantenna at its environment and L is the length of the nanoantenna. Nanofabrication of the metasurface was carried out using electron beam lithography, as detailed in the Supplementary Material. The resulting metasurfaces were characterized via scanning electron microscopy SEM), as shown in Fig. 1 c), and further analyzed using FTIR spectroscopy, which is discussed in Secs. 2.3 and 2.4.

2 3 MEIP Tomography

To visualize the transient thermal dynamics of a metasurface interacting with aqueous solutions, a 3D imaging system is essential for capturing the depth-dependent temperature response. Precise z-axis sectioning is necessary for locating the hot spots of a metasurface, as the nanoantennas have a thickness of only 70 nm. The MEIP tomography system is a 3D pump probe imaging system that integrating photothermal microscopy with

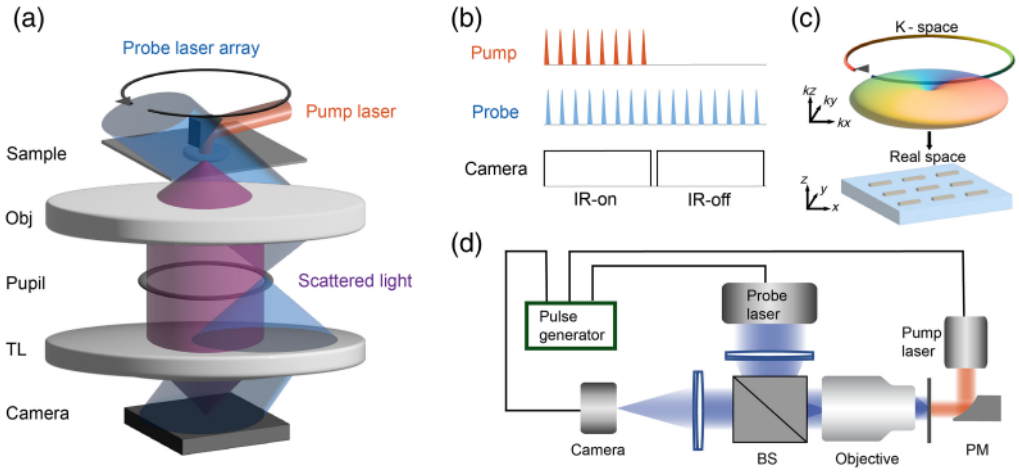

Fig. 2 MEIP tomography setup and reflection MEIP microscopy setup. (a) Schematic of photothermal diffraction tomography setup. TL, tube lens. Obj, objective. The pump beam is illuminated by a mid-IR laser loosely focused with a parabolic mirror. The probe beam consists of a 16-angle fiber diode laser, and the transmitted photons are collected by water immersion objective. IR-on multi-angle images and IR-off multi-angle references are captured by the camera. (b) Synchronization of pump pulses, probe pulses, and camera in the MEIP system. (c) Schematic of intensity diffraction tomography reconstruction. 3D -space information is covered by scanning the illumination angles. 3D refractive index distribution is retrieved by inverse model through Tikhonov regularization. (d) Schematic of reflection MEIP setup. BS, beam splitter. PM, parabolic mirror. Pump mid-IR light was loosely focused by a parabolic mirror onto the sample plane. The probe beam was counter-propagated with a pump and detected with a home-built widefield microscope.

intensity diffraction tomography IDT)[43 45] [Fig. 2 a)]. The IDT system provides 3D refractive index maps with a lateral resolution of 240 nm and an axial resolution of 650 nm. Unlike conventional z-stack imaging, IDT employs multi-angle illumination rather than mechanical stage movement, thus avoiding motion artifacts. The camera captures the interference of the scattered field and the unperturbed illuminating fields. The pump and probe lasers, along with the camera, are synchronized using an "optical boxcar" technique [Fig. 2 b)]. Each camera exposure integrates 500 pulses, enhancing the signal-to-noise ratio of the MEIP measurements. The laser operates at a repetition rate of 5 kHz to accommodate the slow thermal decay of the bulk liquid, resulting in a 3D imaging speed of 3.2 s per volume at each wavenumber. The 4D phase and absorption transfer functions x, y, z, and angle) of the system are derived using the first Born approximation, enabling the retrieval of the 3D complex permittivity distribution via deconvolution of the recorded 2D images [Fig. 2 c)].

2 4 Reflection MEIP Microscope

The depth-resolving capability of the MEIP tomography system allowed us to investigate the contrast mechanism of MEIP signal generation and demonstrate biomolecular sensing. Meanwhile, MEIP sensing can be achieved with a simpler setup using counter-propagating photothermal imaging with a 2D reflection-mode widefield microscope. In the MEIP tomography system, the transmitted photons were collected, so the MEIP signals originated from the temperature-dependent refractive index change of solutions. In the reflection-mode system, temperature modulation of the hot spots alters the effective refractive index of the gold nanoantenna at visible wavelengths, and thus the reflectance of the nanoantenna at visible wavelength is changed. Based on this principle, we built a reflection MEIP microscope by implementing photothermal imaging in a reflection-mode widefield microscope [Fig. 2 d)]. On this counter-propagating pump probe microscope, the QCL pulses, the visible pulses, and the camera are synchronized for virtual lock-in detection of the MEIP signal.

3 Results

3 1 Simulation Results of MEIP Contrast Mechanism

To elucidate the MEIP signal generation mechanism, we performed the simulation of the local IR field and transient local temperature rise for a gold nanoantenna with the plasmonic resonance frequency tuned to 1650 cm ^{1}. Finite-element method simulations of the optical field distribution and thermal dynamics of the nanoantenna immersed in liquid environments were performed using COMSOL. The IR reflectance spectra of the antenna for H_2O and D_2O by the locally enhanced field are shown in Fig. 3 a). The reflectance spectrum of D_2O, with a broad spectral bandwidth 300 cm ^{1}), corresponds to the locally enhanced IR field at each wavenumber. The reflectance spectrum of H_2O shows a characteristic dip at 1640 cm ^{1}, corresponding to the H O H bending vibration. The fidelity of the simulations was validated by comparing the simulated and experimentally measured IR reflectance spectra [Fig. 3 a)]. The slight mismatch between the simulated and experimentally measured spectra is attributed to the difference in incidence angle in the two cases; normal incidence was used in the simulation, whereas a 15× Cassegrain objective with a central obstruction was used in the FTIR-based experimental measurement.

The normalized optical intensity distribution around the nanoantenna at 1650 cm ^{1} shows a localized intensity enhancement of ∼3 orders of magnitude at the nanoantenna tips, as depicted in Fig. 3 b), plotted at the height of 10 nm from the surface of the top layer of gold. This enhancement leads to increased IR absorption by molecules situated in the hot spots. This optical field around the nanoantenna leads to heat generation around the nanoantenna, attributed to two sources [Fig. 3 c)]. First, heat is generated within the gold nanoantenna due to the ohmic loss of the plasmonic resonance. This ohmic loss is predominantly generated around the edges of the nanoantenna, near the center of the antenna along the long axis y-direction). Heat is also generated in water due to the absorption by the vibrational modes of the H_2O molecule, predominantly within the hot spots at the two ends of the nanoantenna. From simulation Fig. S1 in the Supplementary Material), we observe comparable heat generation from ohmic loss within gold and vibrational absorption within a small volume of water 100 nm shell) around the gold antenna.

Next, we performed a heat transfer simulation to understand the thermal dynamics of the metasurface-solution system. The mid-IR pump pulse is approximated by a tophat-shaped input with a pulse width of 250 ns and a peak power of 1.7 mW per unit cell 2.7 μm × 2.7 μm) to match the experiments of MEIP imaging and spectroscopy below. The temperature rise at the end of the heating pulse is mapped in Fig. 3 d). In D_2O, the temperature distribution closely resembles the pattern of ohmic heating in the nanoantenna, where the temperature is higher near the center of the antennas. In H_2O, however, the largest temperature rise occurs within the plasmonic hot spots at the two ends and heat diffuses inward toward the center of the nanoantenna, where the temperature is the lowest. This temperature distribution is notably different from the pattern of heat generation, as seen in Fig. 3 c). This difference between temperature distribution and heat generation results from the high thermal diffusivity of gold $\alpha_{Au} = 1.27 \times 10^{5}$ m^2 s) and CaF_2 $\alpha_{CaF_2} = 3.58 \times 10^{6}$ m^2 s) and the relatively low thermal diffusivity of water $\alpha_{H_2O} = 1.43 \times 10^{7}$ m^2 s). This can be further seen by comparing the heat generation and temperature profile along the long axis of the nanoantenna [Fig. 3 d), dotted green and solid blue curves]. Although the maximum heat generation occurs in water immediately neighboring the gold nanoantenna, corresponding to the location of maximum field intensity, the maximum temperature is reached ∼40 nm away from the gold nanoantenna due to the high heat escape through the gold nanoantenna and CaF_2 substrate.

The high temperature gradients at the hot spots thus introduce an opportunity for the detection of absorbers in the hot spots via the photothermal detection method. We further calculated the spatial and temporal evolution of temperature at the hot spots. A cross-sectional temperature distribution y z plane) of a nanoantenna in H_2O at the end of the heating pulse is shown in Fig. 3 e). Compared with the electromagnetic field distribution [Fig. 3 b)], the temperature profile exhibits a more diffused pattern, spreading over a region ∼150 nm in size, and the temperature rise reaches a maximum of 60 K at roughly 60 nm above the gold nanoantenna. Figure 3 f) presents the temperature at different heights as a function of time. The temperature dynamics exhibit two distinct behaviors based on the distance from the nanoantenna. Near the antenna below 250 nm), a rapid

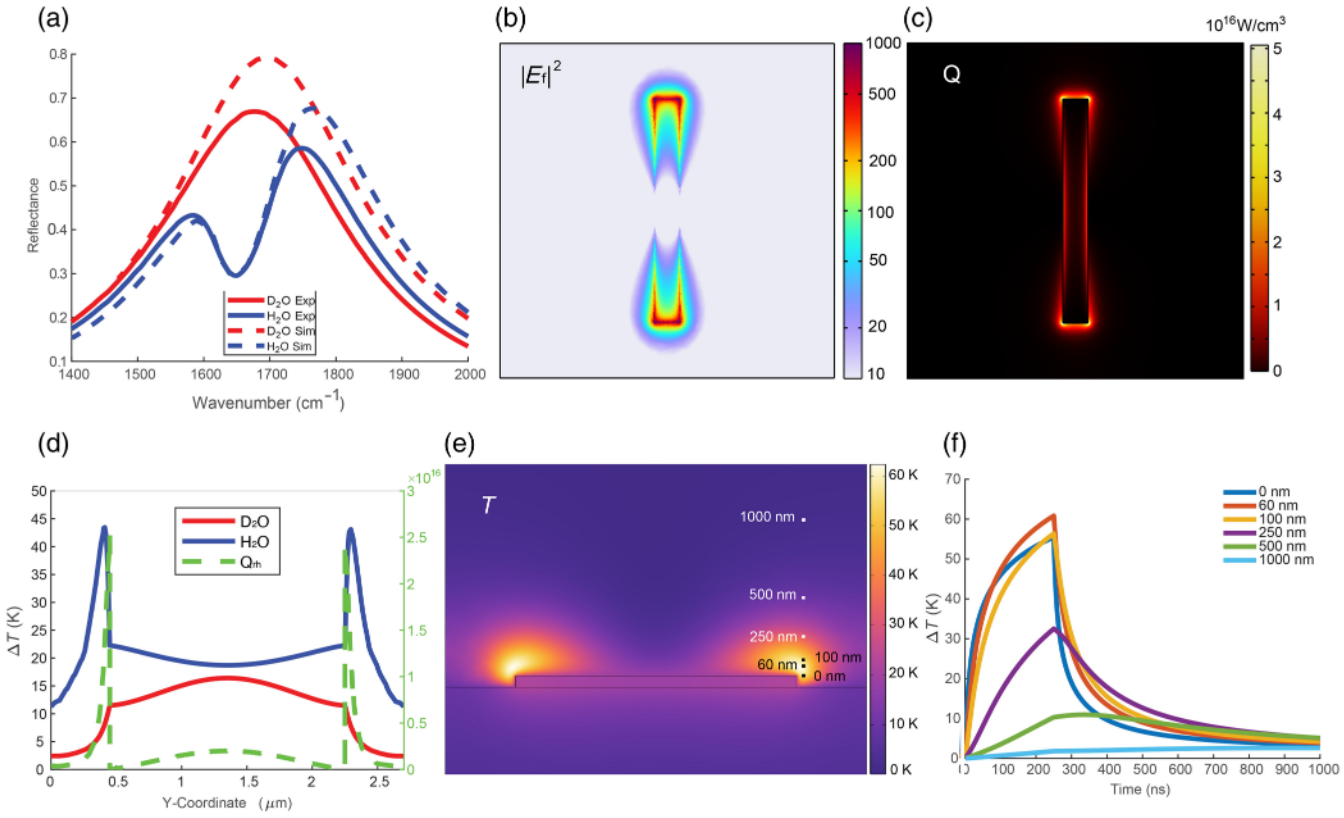

Fig. 3 Simulation of MEIP signal generation. (a) IR reflection spectra of metasurface in H_2O (blue) and D_2O (red) from experiments (solid lines) and simulations (dashed lines). (b) IR intensity enhancement of metasurface excited at 1650 cm ^{1}. (c) Heat dissipation around nanoantenna excited at 1650 cm ^{1}. (d) Line plot of temperature increase (blue, red) and heat dissipation (green) through the center of nanoantenna under a heating pulse of 250 ns at 1650 cm ^{1}. (e) y z cross-sectional map of the temperature distribution in the small volume surrounding nanoantenna at 250 ns. (f) Time-dependent temperature plot at various heights from the gold surface and 40 nm away from the center of nanoantenna tip.

temperature increase is observed due to localized IR absorption by the liquid at the nanoantenna hot spots. This localized heating leads to a steep temperature rise immediately following the pulse and the temperature maximum is reached at the end of the IR pump pulse. The maximum temperature at each position is governed by not only the heat generation the closer to the nanoantenna, the larger the electromagnetic heating) but also the heat dissipation from the nanoantenna and CaF_2 substrate the closer to the nanoantenna, the greater the heat dissipation). This results in a maximum temperature peak observed at 60 nm above the hot spots. On the other hand, further away from the antenna 500 nm and above), the temperature increases more gradually, driven primarily by thermal diffusion from the hot spots into the surrounding liquid. In this region, the maximum temperature is reached with a short delay after the end of the IR pump pulse, depending on the height. After the end of the IR pump pulse, electromagnetic heating stops, and temperature change is entirely due to thermal diffusion within the medium. Cooling occurs close to the nanoantenna, with the cooling rate dependent on the distance from the gold nanoantenna. Cooling is faster the closer a position is to the nanoantenna due to the high thermal diffusivity of gold and CaF_2, whereas the small thermal diffusivity of water tends to slow down this cooling in regions further away from the nanoantenna. Together with thermal diffusion deeper into the water, this effect can shift the maximum temperature deeper into the water and away from the nanoantenna as time progresses.

3 2 Spatial and Temporal Thermal Dynamics at the Metasurface

To experimentally investigate the MEIP process, we conducted photothermal imaging of a metasurface in liquids. The nanoantennas were first immersed in deionized water, as depicted in Fig. 4 a). The IR pump pulse width is 250 ns, consistent with the simulation settings, and the probe pulse width is set to 240 ns to match the pump pulse. The MEIP images obtained in water revealed the 3D heat transfer generated by liquids, whereas the MEIP spectra confirmed the spectroscopic capability of absorbers located at the hot spots. Notably, the maximum temperature layer was observed above the top surface of the gold nanoantenna $z = 0$ μm), consistent with the simulation results shown in Fig. 3 e). The depth-resolved MEIP measurements of nanoantenna in water Fig. S2 in the Supplementary Material) show that the temperature reached its maximum at 200 nm above the gold surface. The offset between the experiment and simulation resulted from the axial resolution limitation of the MEIP system discussed in Sec. 2.3) and the disparity between the temporal

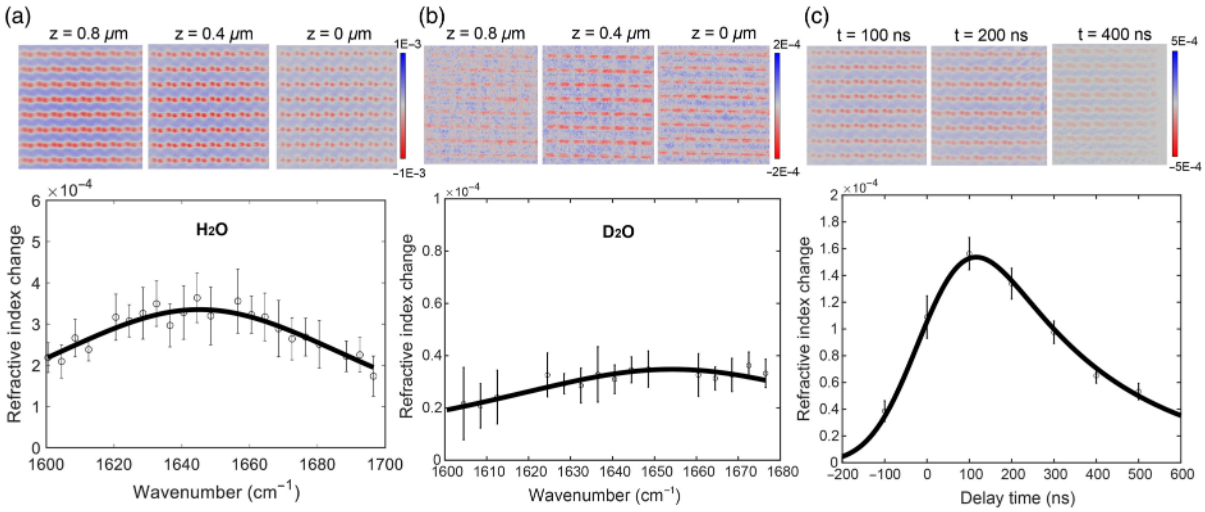

Fig. 4 Photothermal imaging and spectroscopy of metasurface in H_2O and D_2O. (a) Depth-resolved photothermal images and spectra of nanoantenna in water. (b) Depth-resolved photothermal images and spectra of nanoantenna in D_2O. Solid line, Lorentzian fitted curve; error bar, standard deviation of MEIP signals from single nanoantennas ($n = 10$). (c) Time-dependent photothermal images and spectra of nanoantenna in water. Solid line, fitted as a convolution of a Gaussian function and exponential function; error bar, standard deviation of MEIP signals from single nanoantennas ($n = 10$).

profiles of the visible laser pulse and the simulated probe pulse. Beyond $z = 0.8$ μm, the temperature rise is primarily attributed to heat transfer from the hot spots, with a more diffused distribution resulting from thermal diffusion in water. The MEIP spectra of absorbers at the hot spots, presented in Fig. 4 a), were obtained by integrating the photothermal-induced refractive index changes within a cutoff box of 400 nm in diameter centered at the tip of the nanoantenna. By contrast, MEIP imaging of nanoantenna immersed in D_2O demonstrated heat dissipation within the gold nanostructures, with the temperature peaking at the center of the gold [Fig. 4 b)]. The corresponding MEIP spectra for D_2O represent background signals resulting from heat energy generated by the gold nanostructures. A key observation is that the temperature rise in H_2O is ~10 times greater than in D_2O, as shown by comparing the MEIP spectra in Figs. 4 a) and 4 b). This finding aligns with the theoretical estimation, as shown in Fig. 3 d).

We further studied the time evolution of the MEIP signal for nanoantenna in H_2O, as shown in Fig. 4 c) and Fig. S3 in the Supplementary Material. The thermal decay constant was fitted to be 287 ns using the fitting function as a convolution of a Gaussian function instrumental response) and an exponential function thermal decay). These results demonstrate that MEIP imaging and spectroscopy can effectively map the thermal dynamics of the nano-environment, capturing the coupled thermal generation from both the nanostructures and the surrounding liquids in local hot spots. Consequently, the MEIP method holds the potential for infrared sensing of low-abundance molecules in solutions.

To gain a deeper understanding of the thermal-optical response in the MEIP process, we performed MEIP imaging using two different probe wavelengths: 450 and 638 nm, respectively. Given that gold has a negative thermo-optic coefficient at 450 nm and a positive thermo-optic coefficient at 638 nm,[46] the MEIP signals were expected to exhibit opposite contrasts at gold nanoantennas. We compared the MEIP signals from a probe wavelength of 450 nm using the MEIP tomography setup and a probe wavelength of 638 nm using the reflection MEIP setup, detailed in the Supplementary Material. As shown in Fig. S4 in the Supplementary Material, the MEIP image acquired at 638 nm reveals plasmonic hot spots at the ends of each antenna in H_2O and rectangular nanoantennas in D_2O, but with the photothermal signal exhibiting opposite signs in the two media. This is in contrast to the observation at 450 nm Fig. 4), where the plasmonic hot spots in H_2O and rectangular nanoantennas in D_2O are seen with the same sign of refractive index change. This difference is the direct result of a sign change in the thermo-optic coefficient of gold negative at 450 nm and positive at 638 nm), but not that of water negative at both 450 and 638 nm).

3 3 MEIP Sensing of Proteins and Nitrile Molecules

To show the capability of fingerprinting biomolecules at low concentrations, we performed hyperspectral MEIP imaging of protein solutions. We first conducted MEIP spectroscopy on bovine serum albumin BSA) protein at a concentration of 1 mM in water. A droplet of the prepared solution was placed on a metasurface chip fabricated on a CaF_2 substrate, allowing the liquid to rest on the sample for 15 min before conducting the MEIP measurements. The sample was excited using a mid-infrared mid-IR) laser as the pump beam, whereas a 450-nm laser diode array served as the probe beam, co-propagating from the bottom of the CaF_2 substrate [Fig. 5 a)]. The transmitted photons, after interaction with the metasurface-solution sample, were collected using a water immersion objective. The IDT image of the metasurface was reconstructed in Fig. 5 a) inset), where the imaginary part of refractive index is plotted for gold nanoantenna with high absorption at visible wavelengths. Amide-I resonance of BSA protein in water was detected using

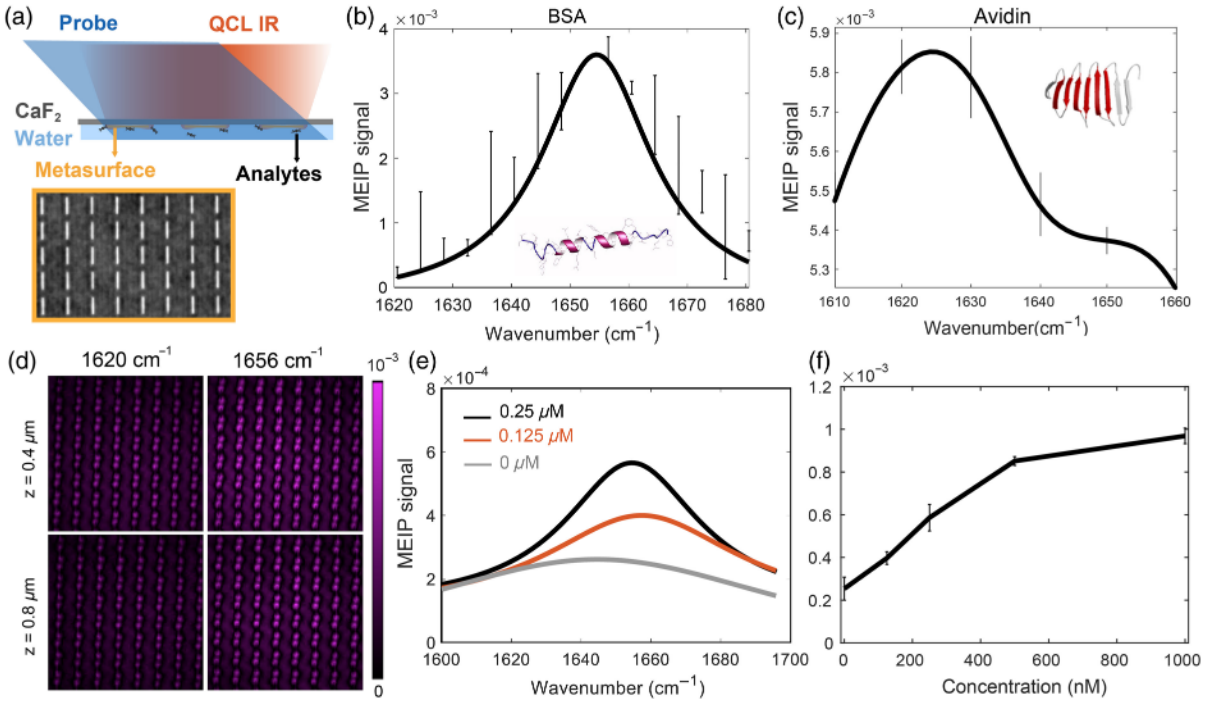

Fig. 5 MEIP sensing of proteins of different secondary structures. (a) Schematic of MEIP sensing with MEIP tomography. (b) MEIP spectra of BSA in water. (c) MEIP spectra of avidin in water. (d) MEIP images of BSA solution at a concentration of 500 nM. (e) MEIP spectra of BSA at various concentrations. Solid line, Lorentzian fitted curve. (f) Concentration-dependence of MEIP signals. Error bar, the standard deviation of MEIP signals from single nanoantennas ($n = 10$).

MEIP, showing a distinct mid-IR peak at 1655 cm ^{1}, fitted with Lorentzian functions [Fig. 5 b)]. The MEIP spectroscopy technique is generally applicable across the fingerprint window of biomolecules, with a characteristic enhancement peak at 1650 cm ^{1}. This capability enables the differentiation of protein secondary structures *in vitro*. For instance, the MEIP spectra of avidin protein [Fig. 5 c)] revealed a mid-IR peak at 1625 cm ^{1}, indicative of β-sheet secondary structures, in contrast to the α-helix-dominant structures observed in BSA.

To experimentally calibrate the sensitivity improvement of MEIP for detecting biomolecules, we performed concentration-dependent MEIP spectroscopy of BSA protein solutions in water [Figs. 5 d) 5 f)]. The temperature maps of the protein solutions displayed a similar distribution to those obtained in pure water, but with stronger signal intensity due to the metasurface enhanced IR absorption by protein molecules localized at the hot spots. The MEIP spectra [Fig. 5 e)] demonstrated a positive correlation between the MEIP signal and the concentration of BSA in water. Specifically, the MEIP spectrum for pure water exhibited a peak at 1640 cm ^{1}, consistent with the vibrational resonance of water. By contrast, the spectra for BSA solutions at varying concentrations showed a peak at 1655 cm ^{1}, corresponding to IR absorption from BSA protein molecules concentrated at the hot spots. The concentration-dependent curve [Fig. 5 f)] displayed a linear relationship at low concentrations below 0.5 μM) before reaching a saturation threshold at higher concentrations. This threshold behavior suggests potential adsorption of BSA on the gold nanoantenna; at the saturation concentration of ~0.5 μM, the local concentration of protein at the gold surface becomes sufficiently high for the molecules to form a fully covered monolayer. The fitted threshold concentration further supports the hypothesis of enhanced IR absorption resulting from densely packed protein molecules within the hot spots.

The dominant contribution to the photothermal signal arises from IR absorption by molecules concentrated at the gold surface rather than freely diffusing ones in solution. However, in the MEIP tomography system, the signal we detect is not direct absorption but rather the modulation of transmitted and scattered photons in the presence of gold nanoantennas, which are highly reflective. Thus, the measured contrast reflects changes in the local scattering potential, primarily influenced by temperature-induced refractive index changes in the gold. In other words, although the BSA-induced temperature rise occurs mainly at the gold surface rather than the surrounding solutions, the MEIP tomography system reports higher contrast at hot spots due to the altered optical properties of gold.

Upon confirmation of the MEIP contrast mechanism and sensing capability using the MEIP tomography system, we further explored sensing with the reflection MEIP microscope. We have designed a new nanoantenna with its plasmonic resonance tuned to 2100 cm ^{1}. We then recorded the MEIP spectra of 2-hydroxybenzonitrile in water at different concentrations. We chose this molecule because nitrile bonds are commonly found in various drug molecules, including anastrozole for breast cancer treatment and vildagliptin and saxagliptin for diabetes medications.[47] The 2-hydroxybenzonitrile molecules were dissolved in water and introduced into the chamber bottomed with a metasurface designed to resonate at 2100 cm ^{1} [Fig. 6 a)]. The concentration-dependent MEIP measurements of 2-hydroxybenzonitrile solutions are presented in Figs. 6 b) and 6 c). With

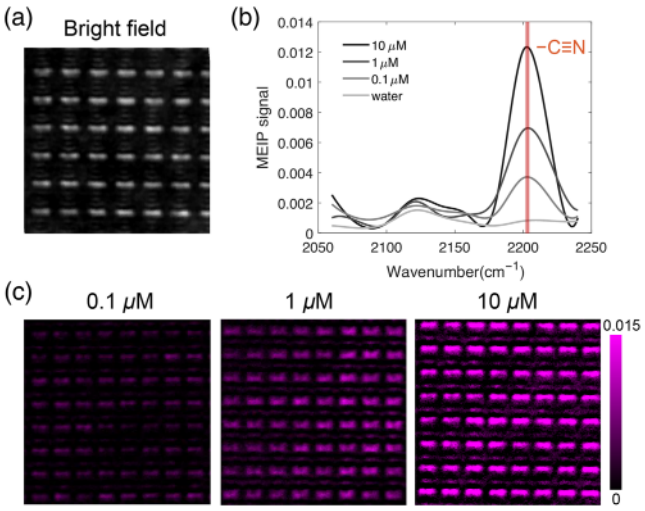

Fig. 6 Sensing of nitrile molecules with reflection MEIP system. (a) Bright-field image of metasurface in nitrile solution. (b) MEIP spectra of nitrile molecules in water with a concentration of 0 to 10 μM. (c) MEIP images of metasurface in nitrile solutions.

the enhanced sensitivity of the metasurface, we achieved a detection limit of 100 nM for nitrile-containing molecules in water, with a characteristic vibrational peak at 2200 cm ^{1}. These results highlight the potential of MEIP microscopy for detecting pharmaceutical compounds in aqueous environments, offering a highly sensitive platform for drug and biomolecular sensing.

4 Discussion

It is striking that MEIP spectra of 125 nM BSA proteins in an aqueous solution show the α-helix peak at 1655 cm ^{1} with a little water background Fig. 5). This result shows the outstanding sensitivity of MEIP microscopy for protein secondary structure analysis. This high sensitivity is primarily attributed to the surface adsorption of BSA on a gold surface, as reflected in the saturation behavior seen in the photothermal signal dependence on BSA concentration. BSA adsorption can be modeled using the Langmuir adsorption model

$$\frac{\text{—}}{\text{—}_{\max}} = \frac{K_{\text{eq}}[\text{BSA}]_{\text{free}}}{1 + K_{\text{eq}}[\text{BSA}]_{\text{free}}}, \tag{4}$$

where $\frac{\text{—}}{\text{—}_{\max}}$ is the fractional surface coverage of BSA on gold, K_{eq} is the equilibrium binding constant of BSA on gold, and $[\text{BSA}]_{\text{free}}$ is the concentration of free BSA in solution. Using this model and our experimental data, we have determined $K_{\text{eq}} = 0.93$ μM ^{1} using our experimental data, which agrees with reported values in the literature in the range of 0.3 to 1 μM ^{1}.$^{48\ 50}$ A detection limit of 125 nM obtained in our experiment corresponds to a fractional surface coverage of 0.24.

The dominant contribution to the photothermal signal originates from BSA adsorbed on the gold surface rather than from free BSA in solution. As the thermal relaxation of these surface-bound BSA molecules is relatively fast, the temperature rise induced by the adsorbed BSA is smaller than it would be if a same number of molecules were located within the plasmonic hot spots in water. Consequently, BSA adsorption may be considered suboptimal for maximizing photothermal detection sensitivity. On the other hand, proteins can be sensitive to thermal denaturation at elevated temperatures. The thermal denaturation of BSA has been observed at 60°C to 70°C by IR spectroscopy through changes in its protein secondary structure,[51] but no such secondary structure change has been observed in our experiment. The adsorption of BSA to the relatively low-temperature gold surface may in part explain the absence of protein denaturation in our experiment. For broader biosensing applications on molecules with lower thermal stability, it is recommended to replace water with deuterium water or other solvents with lower absorption in the mid-IR spectral window to minimize temperature-induced denaturation.

There are spaces to further improve the performance of MEIP microscopy. Future efforts could focus on further improving heat localization through optimized nanoantenna designs to enhance sensitivity and spatial resolution. In addition, MEIP s potential for high-speed, high-throughput multiplexed infrared spectroscopy positions it as a powerful tool for applications ranging from fingerprint-region biomolecular analysis to cell-silent window studies of drug molecules. This versatility makes MEIP a promising platform for advanced infrared sensing in biomedical research and pharmaceutical development.

5 Conclusion

The reported MEIP system offers a far-field imaging approach to explore the photothermal response in a metasurface system. Our results underscore the critical role of nanoantenna-mediated localized heating in significantly enhancing photothermal detection. By capturing the temperature dynamics at the single-antenna level, MEIP provides a precise understanding of localized thermal effects, which is crucial for optimizing performance. The demonstrated detection of bovine serum albumin at a concentration of 125 nM and nitrile molecules at a concentration as low as 100 nM highlights the extraordinary sensitivity of this method for detecting low-abundance biomolecules in liquid environments. Moreover, the single-antenna sensing capability of MEIP enables spatially resolved infrared spectroscopy, making it suitable for studying molecular interactions at nanoscale hot spots. This unique feature opens new opportunities for multiplexed IR sensing, where individual nanoantennas can be tailor-designed to function as independent sensing units.

Disclosures

The authors declare no financial interests, commercial affiliations, or other potential conflicts of interest that could have influenced the objectivity of this research or the writing of this paper.

Code and Data Availability

All data are available in the main text or the Supplementary Material.

Author Contributions

J. X. C. and G. S. initiated the project. D. J. and S. H. H. conceived the experiments. D. J. and D. D. built the MEIP setup. D. J. conducted the MEIP experiments. D. J. and S. H. H. analyzed the results. S. H. H. and D. T. fabricated and characterized the metasurface. D. T. and S. H. H. performed the simulations. All authors read the manuscript.

Acknowledgments

This work is supported by Grant Nos. R35GM136223 and R33CA287046 to JXC, by Grant Nos. R21CA251052 and R21GM138947 to GS, and in part by Grant No. 2023-321163 from the Chan Zuckerberg Initiative DAF, an advised fund of the Silicon Valley Community Foundation. The fabrication of the plasmonic metasurfaces was performed in part at the Cornell NanoScale Science and Technology Facility CNF), a member of the National Nanotechnology Coordinated Infrastructure NNCI), which is supported by the National Science Foundation Grant No. NNCI-2025233).

References

1. I. W. Levin and R. Bhargava, "Fourier transform infrared vibrational spectroscopic imaging: integrating microscopy and molecular recognition," *Annu. Rev. Phys. Chem.* **56**, 429 474 2005).
2. M. J. Baker et al., "Using Fourier transform IR spectroscopy to analyze biological materials," *Nat. Protoc.* **9**, 1771 1791 2014).
3. R. Bhargava, "Infrared spectroscopic imaging: the next generation," *Appl. Spectrosc.* **66**, 1091 1120 2012).
4. C. K. Akhgar et al., "The next generation of IR spectroscopy: EC-QCL-based mid-IR transmission spectroscopy of proteins with balanced detection," *Anal. Chem.* **92**, 9901 9907 2020).
5. R. Adato et al., "Ultra-sensitive vibrational spectroscopy of protein monolayers with plasmonic nanoantenna arrays," *Proc. Natl. Acad. Sci.* **1 6**, 19227 19232 2009).
6. R. Adato and H. Altug, "*In situ* ultra-sensitive infrared absorption spectroscopy of biomolecule interactions in real time with plasmonic nanoantennas," *Nat. Commun.* **4**, 2154 2013).
7. C. Wu et al., "Fano-resonant asymmetric metamaterials for ultrasensitive spectroscopy and identification of molecular monolayers," *Nat. Mater.* **11**, 69 75 2012).
8. A. John-Herpin, A. Tittl, and H. Altug, "Quantifying the limits of detection of surface-enhanced infrared spectroscopy with grating order-coupled nanogap antennas," *ACS Photonics* **5**, 4117 4124 2018).
9. F. Neubrech et al., "Surface-enhanced infrared spectroscopy using resonant nanoantennas," *Chem. Rev.* **117**, 5110 5145 2017).
10. S. H. Huang et al., "Metasurface-enhanced infrared spectroscopy in multiwell format for real-time assaying of live cells," *Lab Chip* **23**, 2228 2240 2023).
11. D. Etezadi et al., "Nanoplasmonic mid-infrared biosensor for *in vitro* protein secondary structure detection," *Light Sci. Appl.* **6**, e17029 2017).
12. L. Dong et al., "Nanogapped Au antennas for ultrasensitive surface-enhanced infrared absorption spectroscopy," *Nano Lett.* **17**, 5768 5774 2017).
13. K. Aleshire et al., "Far-field midinfrared superresolution imaging and spectroscopy of single high aspect ratio gold nanowires," *Proc. Natl. Acad. Sci.* **117**, 2288 2293 2020).
14. S. A. Hosseini Jebeli et al., "Wavelength-dependent photothermal imaging probes nanoscale temperature differences among subdiffraction coupled plasmonic nanorods," *Nano Lett.* **21**, 5386 5393 2021).
15. P. E. Batson, "Applied physics. Plasmonic modes revealed," *Science* **335**, 47 48 2012).
16. B. Knoll and F. Keilmann, "Near-field probing of vibrational absorption for chemical microscopy," *Nature* **399**, 134 137 1999).
17. R. Esteban et al., "Direct near-field optical imaging of higher order plasmonic resonances," *Nano Lett.* **8**, 3155 3159 2008).
18. P. Alonso-Gonzalez et al., "Visualizing the near-field coupling and interference of bonding and anti-bonding modes in infrared dimer nanoantennas," *Opt. Express* **21**, 1270 1280 2013).
19. A. Dazzi and C. B. Prater, "AFM-IR: technology and applications in nanoscale infrared spectroscopy and chemical imaging," *Chem. Rev.* **117**, 5146 5173 2017).
20. A. Dazzi et al., "Local infrared microspectroscopy with subwavelength spatial resolution with an atomic force microscope tip used as a photothermal sensor," *Opt. Lett.* **3** , 2388 2390 2005).
21. F. Lu, M. Jin, and M. A. Belkin, "Tip-enhanced infrared nanospectroscopy via molecular expansion force detection," *Nat. Photonics* **8**, 307 312 2014).
22. P. Alonso-Gonzalez et al., "Real-space mapping of Fano interference in plasmonic metamolecules," *Nano Lett.* **11**, 3922 3926 2011).
23. B. Lahiri et al., "Nanoscale imaging of plasmonic hot spots and dark modes with the photothermal-induced resonance technique," *Nano Lett.* **13**, 3218 3224 2013).
24. A. B. Khanikaev et al., "Experimental demonstration of the microscopic origin of circular dichroism in two-dimensional metamaterials," *Nat. Commun.* **7**, 12045 2016).
25. D. Zhang et al., "Depth-resolved mid-infrared photothermal imaging of living cells and organisms with submicrometer spatial resolution," *Sci. Adv.* **2**, e1600521 2016).
26. Z. Li et al., "Super-resolution far-field infrared imaging by photothermal heterodyne imaging," *J. Phys. Chem. B* **121**, 8838 8846 2017).
27. D. Zhang et al., "Bond-selective transient phase imaging via sensing of the infrared photothermal effect," *Light Sci. Appl.* **8**, 116 2019).
28. Y. Bai, J. Yin, and J. X. Cheng, "Bond-selective imaging by optically sensing the mid-infrared photothermal effect," *Sci. Adv.* **7**, eabg1559 2021).
29. Q. Xia et al., "Mid-infrared photothermal microscopy: principle, instrumentation, and applications," *J. Phys. Chem. B* **126**, 8597 8613 2022).
30. J. Yin et al., "Video-rate mid-infrared photothermal imaging by single-pulse photothermal detection per pixel," *Sci. Adv.* **9**, eadg8814 2023).
31. X. Teng et al., "Mid-infrared photothermal imaging: instrument and life science applications," *Anal. Chem.* **96**, 7895 7906 2024).
32. H. He et al., "Mapping enzyme activity in living systems by real-time mid-infrared photothermal imaging of nitrile chameleons," *Nat. Methods* **21**, 342 352 2024).
33. Q. Xia et al., "Single virus fingerprinting by widefield interferometric defocus-enhanced mid-infrared photothermal microscopy," *Nat. Commun.* **14**, 6655 2023).
34. Y. Bai et al., "Ultrafast chemical imaging by widefield photothermal sensing of infrared absorption," *Sci. Adv.* **5**, eaav7127 2019).
35. E. M. Paiva and F. M. Schmidt, "Ultrafast widefield mid-infrared photothermal heterodyne imaging," *Anal. Chem.* **94**, 14242 14250 2022).
36. H. Zong et al., "Background-suppressed high-throughput mid-infrared photothermal microscopy via pupil engineering," *ACS Photonics* **8**, 3323 3336 2021).
37. M. Tamamitsu et al., "Label-free biochemical quantitative phase imaging with mid-infrared photothermal effect," *Optica* **7**, 359 366 2020).
38. J. Zhao et al., "Bond-selective intensity diffraction tomography," *Nat. Commun.* **13**, 7767 2022).
39. H. Zong et al., "Bond-selective full-field optical coherence tomography," *Opt. Express* **31**, 41202 41218 2023).
40. D. Jia et al., "3D chemical imaging by fluorescence-detected mid-infrared photothermal Fourier light field microscopy," *Chem. Biomed. Imaging* **1**, 260 267 2023).
41. R. Semenyshyn et al., "Pushing down the limit: *in vitro* detection of a polypeptide monolayer on a single infrared resonant nanoantenna," *ACS Photonics* **6**, 2636 2642 2019).

42. C. Huck et al., "Plasmonic enhancement of infrared vibrational signals: nanoslits versus nanorods," *ACS Photonics* **2**, 1489 1497 2015).
43. L. Tian, J. Wang, and L. Waller, "3D differential phase-contrast microscopy with computational illumination using an LED array," *Opt. Lett.* **39**, 1326 1329 2014).
44. A. Matlock and L. Tian, "High-throughput, volumetric quantitative phase imaging with multiplexed intensity diffraction tomography," *Biomed. Opt. Express* **1** , 6432 6448 2019).
45. J. Li et al., "High-speed *in vitro* intensity diffraction tomography," *Adv. Photonics* **1**, 066004 2019).
46. T. Favaloro, J. H. Bahk, and A. Shakouri, "Characterization of the temperature dependence of the thermoreflectance coefficient for conductive thin films," *Rev. Sci. Instrum.* **86**, 024903 2015).
47. F. F. Fleming et al., "Nitrile-containing pharmaceuticals: efficacious roles of the nitrile pharmacophore," *J. Med. Chem.* **53**, 7902 7917 2010).
48. S. H. Brewer et al., "Probing BSA binding to citrate-coated gold nanoparticles and surfaces," *Langmuir* **21**, 9303 9307 2005).
49. P. Roach, D. Farrar, and C. C. Perry, "Interpretation of protein adsorption: surface-induced conformational changes," *J. Am. Chem. Soc.* **127**, 8168 8173 2005).
50. D. H. Tsai et al., "Adsorption and conformation of serum albumin protein on gold nanoparticles investigated using dimensional measurements and *in situ* spectroscopic methods," *Langmuir* **27**, 2464 2477 2011).
51. S. Vijayakumar et al., "Laser-based mid-infrared spectroscopy for monitoring temperature-induced denaturation of bovine serum albumin and de-/stabilization effects of sugars," *Anal. Chem.* **95**, 6441 6447 2023).

Danchen Jia received her BS degree in optical science and engineering from Zhejiang University, China (2020). She is currently a PhD student with Prof. Ji-Xin Cheng at Boston University, USA. Her research interests focus on optical microscopy, label-free spectroscopy and plasmonic metasurfaces.

Steven H. Huang received his BS degree in engineering science from the University of Toronto, Canada (2010), his MS degree in electrical engineering from Stanford University, USA (2012), and his PhD in electrical engineering from Washington University in St. Louis, USA (2018). He is currently a research associate with Prof. Gennady Shvets at Cornell University, USA. His research interests focus on metasurfaces, infrared spectroscopy, and microscopy.

Dias Tulegenov received his BS degree in physics from Nazarbayev University, Kazakhstan (2022). He is currently a PhD student with Prof. Gennady Shvets in applied and engineering physics at Cornell University. His research interests focus on plasmonic metasurfaces and infrared spectroscopy.

Dashan Dong received his BS degree in applied physics from Nankai University (2014) and his PhD in optics from Peking University (2019). He is currently a post-doctoral researcher in Prof. Ji-Xin Cheng s group at Boston University, where he develops and deploys label-free optical imaging techniques for biomedical applications. His broader research interests include computational microscopy, quantitative phase imaging, and the label-free characterization of living systems.

Gennady Shvets is a professor of applied and engineering physics at Cornell University and director of the Cornell Laboratory for Plasma Studies (LPS). He received his PhD in physics from MIT in 1995. His research interests include nanophotonics, optical and microwave metamaterials and their applications (including bio-sensing, optoelectronic devices, and vacuum electronics), topological concepts in photonics, and plasma physics.

Ji-Xin Cheng is the Moustakas Chair Professor of Photonics and Optoelectronics, affliated with Departments of Biomedical Engineering and Electrical Computer Engineering at Boston University. He received his PhD from the University of Science and Technology of China in 1998. His research interests include optical imaging, cancer diagnostics, neuromodulation, and phototherapy for infectious diseases.